Electronic Compressibility of Magic-Angle Graphene Superlattices

S. L. Tomarken, Y. Cao, A. Demir, K. Watanabe, T. Taniguchi, P. Jarillo-Herrero, and R. C. Ashoori

Phys. Rev. Lett. **123**, 046601 — Published 24 July 2019

DOI: 10.1103/PhysRevLett.123.046601

Electronic compressibility of magic-angle graphene superlattices

S.L. Tomarken,[1] Y. Cao,[1] A. Demir,[1] K. Watanabe,[2] T. Taniguchi,[2] P. Jarillo-Herrero,[1,*] and R.C. Ashoori[1,†]

[1] *Department of Physics, Massachusetts Institute of Technology, Cambridge, MA 02139*
[2] *National Institute of Materials Science 1-1 Namiki, Tsukuba 305-0044, Japan*

We report the first electronic compressibility measurements of magic-angle twisted bilayer graphene. The evolution of the compressibility with carrier density offers insights into the interaction-driven ground state that have not been accessible in prior transport and tunneling studies. From capacitance measurements, we determine chemical potential as a function of carrier density and find the widths of the energy gaps at fractional filling of the moiré lattice. In the electron-doped regime, we observe unexpectedly large gaps at quarter- and half-filling and strong electron–hole asymmetry. Moreover, we measure a ∼35 meV mini-bandwidth that is much wider than most theoretical estimates. Finally, we explore the field dependence up to the quantum Hall regime and observe significant differences from transport measurements.

In most metals, interactions between electrons are sufficiently weak compared with electronic kinetic energy that they can be considered as a perturbation when calculating band structure. Because the kinetic energy of an electronic system is proportional to the bandwidth of its low energy bands, one route to finding materials with effectively strong electron–electron interactions is to study systems with flat energy dispersions. Stacking and rotating two monolayers of graphene by a controllable angle between the two layers can tune the resulting low-energy band structure through a large range of energy dispersion [1–3]. At certain small twist angles known as *magic angles*, the interlayer hybridization energy concentrates the low-energy density of states within about 10 meV according to calculations [1, 3], providing a highly tunable test bed for strongly correlated physics.

Early scanning tunneling spectroscopy (STS) measurements on twisted bilayer graphene revealed van Hove singularities in the low-energy moiré bands for low twist angle samples [4]. More recent experiments show anomalous insulating behavior in magic-angle twisted bilayer graphene (MATBG) around $n = \pm n_s/2$, where n_s is the electron density at which the low-energy superlattice bands are completely filled (four electrons per moiré cell). The insulating behavior has features similar to those expected for a Mott insulator arising from on-site Coulomb repulsion [5], though there are currently many theoretical proposals for various strongly correlated phases [6–19]. Strikingly, superconductivity was also observed around $n = -n_s/2$ (two holes per supercell) with density-dependent critical temperatures up to 1.7 K [20].

In order to probe the thermodynamic ground state of MATBG, we use a low-temperature capacitance bridge to access the electronic compressibility of the two devices originally characterized with transport in Ref. 20. By measuring the compressibility as a function of carrier density, we study the thermodynamic evolution of the interaction-driven phases at fractional filling, offering new insights into the nature of the MATBG ground state that complement previous transport [5, 20–24] and tunneling efforts [25, 26]. Additionally, we can extract the thermodynamic bandwidth of the low energy bands, enabling us to evaluate their relative flatness and compare to electronic structure calculations. Figure 1 shows the device geometry and measurement schematic. MATBG samples were fabricated using a "tear-and-stack" technique [27, 28]. The MATBG is encapsulated between two layers of hexagonal boron nitride (hBN) and placed on top of a local, metal back gate. The structures were etched into a Hall geometry for initial transport measurements in Ref. 20. However, in our capacitance measurements, we electrically short all contacts together to reduce the RC charging time of the devices [29].

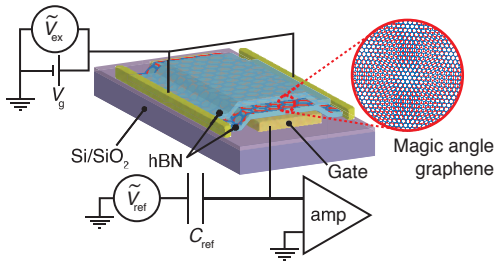

FIG. 1. Schematic of MATBG device and capacitance bridge measurement scheme.

We apply an AC excitation to the MATBG contacts and a balancing AC excitation of variable phase and amplitude to a ∼45 fF reference capacitor connected to the back gate in a bridge configuration as shown in Fig. 1. We measure small changes in the sample impedance by monitoring off-balance voltage accumulation at the balance point, and we model the total capacitance C_T of the MATBG structure after subtraction of a constant background (see Supplemental Material for details) as consisting of two contributions: $C_T^{-1} = C_{geo}^{-1} + C_q^{-1}$. C_{geo} is the geometric capacitance arising from the parallel

* Correspondence to: pjarillo@mit.edu
† Correspondence to: ashoori@mit.edu

plate geometry of the MATBG and local back gate while $C_q = Ae^2\partial n/\partial\mu$ is the quantum capacitance [30] which is directly proportional to the thermodynamic compressibility $\partial n/\partial\mu$ (A is the lateral device area and e is the elementary charge). By measuring modulation of the capacitance as a function of gate voltage and magnetic field, we detect the presence of gaps in the thermodynamic density of states. Importantly, we restrict our measurements to sufficiently low frequencies to ensure that modulation of the measured signal arises entirely from changes of the electronic compressibility and does not result from charging-rate effects [31]. At high magnetic field, where the in-plane resistance becomes appreciable, we restrict ourselves to a qualitative discussion of the field-induced gaps [32].

Figure 2(a) and (b) show capacitance measurements (red traces) at zero magnetic field for the two devices (M2 and M1) that previously showed unexpected insulating and superconducting phases in Ref. 20. Devices M2 and M1 were found previously to have twist angles of 1.05° and 1.16°, respectively [20]. In both samples, we observe a Dirac-like feature at charge neutrality accompanied by broad, incompressible regions around $\pm 3 \times 10^{12}/\mathrm{cm}^2$, which correspond to either four electrons ($+n_s$) or four holes ($-n_s$) per moiré cell. We observe incompressible phases around $n_s/2$ (two electron per moiré cell) in both devices and a smaller feature around $-n_s/2$ in device M2. These incompressible features correspond to the previously reported insulating phases observed around $\pm n_s/2$ in Ref. 20, however, in our measurement we find that the hole-doped state is significantly less incompressible despite comparable conductance values reported previously. Our results are consistent with more recent transport measurements in which resistive phases in the electron-doped regime are generally stronger than their hole-doped counterparts [21–24].

In both devices we find incompressible phases at $n_s/4$ and weak incompressible features at $-n_s/4$ in device M2. Importantly, the incompressible features at $n_s/4$ and $n_s/2$ are comparable in magnitude despite a lack of insulating temperature-dependence at $n_s/4$ reported previously [20, 21, 23]. In device M2, raising the temperature to 5 K, the highest temperature accessed, produced virtually no change in the capacitance features at commensurate filling (see Supplemental Material). We see no strong compressibility features around $\pm 3n_s/4$ in contrast to recent transport studies [20–24], although, we observe a gradual decrease in capacitance around $\pm 3n_s/4$ as the system enters the superlattice band gaps which makes observation of incompressible features difficult to distinguish in this region.

After subtracting a constant background capacitance C_{back} (see Supplemental Material), the relationship

$$C_T^{-1} = C_{\mathrm{geo}}^{-1} + \left(Ae^2\partial n/\partial\mu\right)^{-1} \tag{1}$$

can be used to extract properties related to the compressibility $\partial n/\partial\mu$. At low temperatures the compressibility can be approximated well by the zero-temperature density of states. For a Dirac-like system with eight-fold degeneracy arising from spin, valley, and layer degrees of freedom, the density of states is given by

$$\frac{\partial n}{\partial\mu} = \frac{4\,|E_F|}{\pi(\hbar v_F)^2} = \frac{2\sqrt{2}}{\sqrt{\pi}\hbar v_F}\sqrt{|n|}. \tag{2}$$

In order to take into account broadening due to the disorder profile across the lateral extent of the sample, we convolve Eq. 2 with a gaussian $g(n) = e^{-n^2/2\Gamma^2}/(\sqrt{2\pi}\Gamma)$ where Γ characterizes the scale of the charge density broadening. We fit our capacitance data using Eq. 1 and

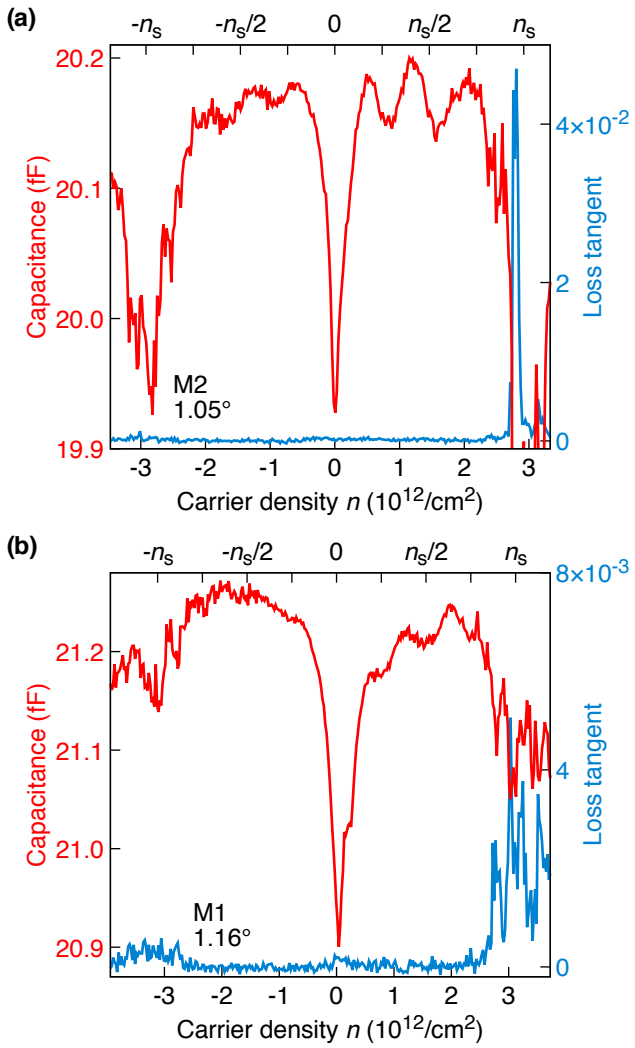

FIG. 2. **(a)** Plot of the capacitance (red trace) and loss tangent (blue trace) of device M2 as a function of carrier density at zero magnetic field and 280 mK. Dips in the capacitance around $n_s/4$ and $n_s/2$ correspond to incompressible phases. Smaller dips around $-n_s/4$ and $-n_s/2$ also show incompressible features. **(b)** Capacitance and loss tangent of device M1 at zero magnetic field and 225 mK. Similar incompressible features are seen at $n_s/4$ and $n_s/2$.

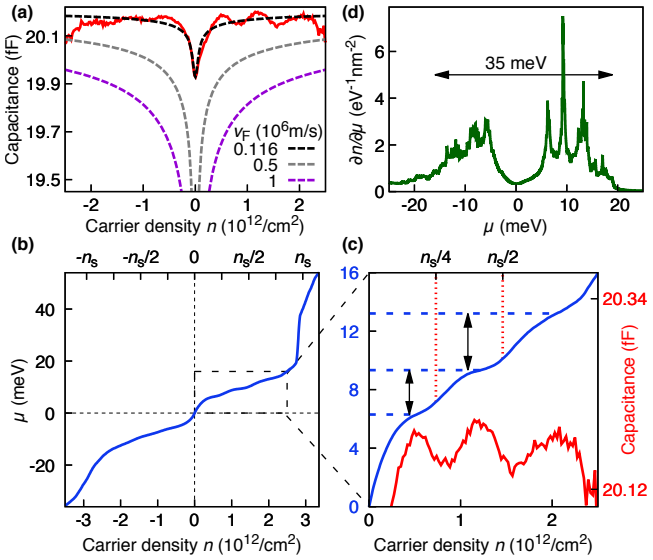

FIG. 3. **(a)** Fits of the capacitance data for sample M2. The Dirac point is best fit by $v_F = 0.116 \times 10^6$ m/s. **(b)** Shift of chemical potential of M2 as a function of carrier density calculated from integrating the inverse quantum capacitance. **(c)** Zoom-in to boxed region of (b). The increase in the chemical potential between the density of states maxima at both $n_s/4$ and $n_s/2$ is shown on the left axis with capacitance data from Fig. 2(a) replotted on the right axis. Arrows correspond to measured $\Delta\mu$ between density of states maxima. We find $\Delta_{n_s/4} = (3.0 \pm 1.0)$ meV and $\Delta_{n_s/2} = (3.9 \pm 1.2)$ meV. **(d)** Extracted compressibility from the capacitance data in Fig. 2(a) as a function of the electronic chemical potential. Arrow is 35 meV wide.

$\partial n/\partial\mu * g(n)$ and determine v_F, Γ, and C_{geo} from a best-fitting procedure. We estimate the area A from the lithographic dimensions of the MATBG flake that lies over the back gate. The capacitance data from sample M2 is best fit by $v_F = 0.116 \times 10^6$ m/s and $\Gamma = 4.0 \times 10^{10}$/cm^2, both of similar magnitude to the values extracted previously with a different sample (1.08°) [5]. Figure 3(a) shows the capacitance data from M2 overlaid with the model evaluated at various values of v_F.

The shift of the chemical potential as carriers are added to the device can be extracted by integrating the inverse quantum capacitance $\Delta\mu = \int \frac{\partial\mu}{\partial n} dn = \int Ae^2 \left(C_T^{-1} - C_{geo}^{-1}\right) dn$. Figure 3(b) shows the calculated chemical potential as a function of carrier density for device M2. Portions of the trace with relatively flat slope correspond to compressible phases where the chemical potential shifts relatively little as carriers are added to the system whereas steeper regions correspond to reductions in the density of states. The superlattice band gaps around $\pm n_s$ manifest as the steep slopes near $n = \pm 3 \times 10^{12}$/cm^2. On the electron side, where the size of the capacitance dips is appreciable, the thermodynamic gap between the density of states peaks can be calculated for both $n_s/4$ and $n_s/2$ as shown in Fig. 3(c). We find $\Delta_{n_s/4} = (3.0 \pm 1.0)$ meV and $\Delta_{n_s/2} = (3.9 \pm 1.2)$ meV, where the error associated with the gap estimation arises from a systematic error in the determination of C_{geo}. See Supplemental Material for a discussion of the error estimation and its propagation in the thermodynamic gap measurements. The gap at $n_s/4$ was either not observed previously [5, 20, 25, 26], found to have non-activated temperature dependence [21, 23], or the resistive feature was not discussed in detail [22]. A recent transport study reported simply-activated temperature dependence at quarter-filling with a gap value of 0.14 meV, though the presence of a gap at charge neutrality may indicate that the twisted bilayer graphene is aligned with the hBN substrate [24]. Our estimate of $\Delta_{n_s/2}$ is significantly larger than the previously reported values of 0.31 meV in Ref. 5, ∼1.5 meV in Ref. 21, and 0.37 meV in Ref. 24

We expect the gap extracted from thermodynamic compressibility to be larger than the activation gap measured through the temperature dependence of the resistivity. As temperature is increased, the electron–electron correlations that create the many-body gap may weaken, causing the gap to decrease as a function of temperature and leading to an underestimation in activation measurements. By measuring at a fixed, low temperature, the gap derived from compressibility is potentially larger. Additionally, there may be a large density of charge carriers that can be thermally excited across the many-body gap at energies that are closer to the Fermi level than the density of states maxima, leading to a smaller activation gap. If we measure the shift in chemical potential just around the steepest portions of trace in Fig. 3(c), we find values of approximately 2 meV and 2.5 meV for the $n_s/4$ and $n_s/2$ states, respectively, which may compare more directly to activation measurements.

We can also make a comparison to recent STS measurements in which splittings of the van Hove singularity at $n_s/2$ of roughly 7.5 meV [25] and 4−8 meV [26] have been measured. Because the STM tip is placed over a clean, atomically resolved region of the sample, the effects of disorder averaging are avoided, leading to a potentially larger observed spectroscopic gap. We note that the van Hove singularity separation when the Fermi level lies at half-filling as seen in STS measurements differs qualitatively from the chemical potential separation observed in compressibility. In the latter case, the carrier density and the band structure itself vary as the Fermi level is raised due to density-dependent electron–electron interactions. Additionally, STS measures the single particle density of states which is a different quantity from the thermodynamic density of states $\partial n/\partial\mu$ accessed in our measurements.

We plot the compressibility $\partial n/\partial\mu = \frac{1}{Ae^2}\left(C_T^{-1} - C_{geo}^{-1}\right)^{-1}$ as shown in Fig. 3(d). The vertical scale of the compressibility is very sensitive to

the precise value of C_{geo}, particularly the highly compressible phases in which $C_{\mathrm{T}} \approx C_{\mathrm{geo}}$. Nonetheless, the horizontal axis is much less sensitive to variation in C_{geo}, and we estimate the bandwidth of the two low-energy moiré bands as 35 meV. If we vary the precise value of C_{geo} over an estimated uncertainty (see Supplemental Material for details), the bandwidth varies from as small as 25 meV to as large as 45 meV. This range of values is much larger than initial calculations for a rotation angle of 1.05° [1, 3, 5], but it is consistent with the 41 meV separation of the valence and conduction band van Hove singularities predicted by recent tight-binding calculations and the 55 meV separation observed by STS for a slightly larger rotation angle of 1.10° [25].

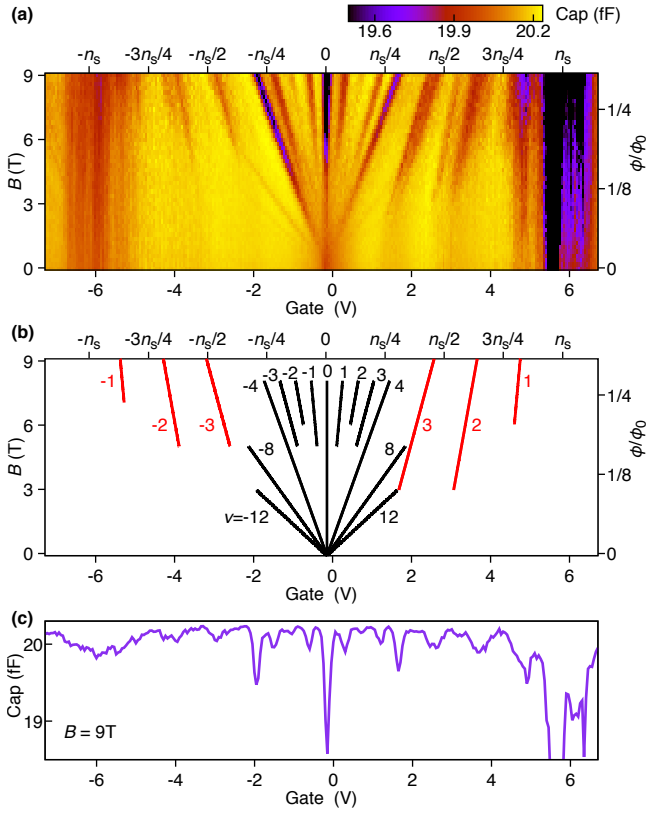

FIG. 4. **(a)** Capacitance as a function of gate voltage and perpendicular magnetic field. Color scale has been suppressed below 19.5 fF in order to show more detail. **(b)** Map of observed gaps in magnetic field measurement in (a). Black traces indicate cyclotron and exchange gaps arising from charge neutrality with the filling factor labeled. Red traces indicate gaps emanating from high magnetic field due to "Hofstadter" replica minibands. **(c)** Capacitance linecut at $B = 9\,\mathrm{T}$ from panel (a).

We also measure the evolution of the compressibility with magnetic field up to the quantum Hall regime. In Fig. 4(a) we plot the capacitance as a function of gate voltage and magnetic field. The incompressible phases at commensurate filling of the miniband do not appear to change with perpendicular magnetic field up to about 3 T after which field-induced gaps arise and coexist, making it difficult to track the relatively broader features associated with the zero-field incompressible phases. The most prominent feature in Fig. 4(a) is a four-fold degenerate Landau fan that emerges from charge neutrality. Despite anticipating an eight-fold degenerate zero energy LL arising from spin, valley, and layer degrees of freedom, our system never develops a compressible phase at charge neutrality, indicating that layer or valley symmetry breaking is present even at zero magnetic field. Four-fold degeneracy may be evidence of C_3 rotational symmetry breaking as recently proposed [33]. At larger magnetic fields we observe incompressible phases at filling factors within the lowest LL octet. These additional incompressible phases presumably arise from exchange-driven gaps as reported in monolayer and bilayer graphene [34–39]. In addition, LLs emerging from the superlattice gaps of device M2 are apparent in Fig. 4(a) as well as from device M1 in Fig. S6(a) in the Supplemental Material.

Additionally, we see a set of gaps emerging from high magnetic field whose intercepts terminate near the fractional filling densities as indicated by the red traces in Fig. 4(b). These gaps appear to form as a result of "Hofstadter" fractal minibands [40, 41]. Similar features have been observed extensively in aligned graphene–hBN structures [42–44] as well as twisted bilayer graphene devices [28, 45]. In Fig. 4(a) some of the gaps which approach commensurate filling appear doubled, suggesting there may be multiple regions within the device with slightly different twist angle. The number of flux quanta per moiré unit cell is plotted on the right vertical axes in Fig. 4(a) and (b). The incompressible phases shown in red in panel Fig. 4(b) intersect at $\phi/\phi_0 = 1$ which occurs at $B = 29.64\,\mathrm{T}$ for $\theta = 1.05°$. Unlike Ref. 21, where no Landau fan was observed emanating from $-n_s/4$, we observe an incompressible phase emerge from high magnetic field whose intercept terminates at $-n_s/4$. Additionally, we observe an incompressible phase emanating from $n_s/4$ corresponding to $\nu = 3$ and not $\nu = 1$ as seen previously [21]. See Supplemental Material for a Wannier diagram and loss tangent in Fig. S5 as well as the field dependence of device M1 with similar features in Fig. S6. The presence of strong quantum oscillations at low magnetic field close to commensurate filling in transport [20, 21, 24] indicates the formation of an emergent Fermi surface and its quantization in magnetic field. Oscillations in transport measurements reflect the field dependence of both the scattering time τ as well as the density of available charge carriers. Because low-frequency capacitance measurements are insensitive to changes in the scattering rate, strong features are not expected when Landau quantization is weak which may explain the lack of low-field capacitance oscillations in our data in contrast with transport [20, 21].

Although there is no consensus on the nature of the

commensurate insulating phases, our results allow us to comment on a few recent proposals. One effort posits that the correlated insulating phase at half-filling is not a Mott-like insulator, but rather a Wigner crystal in which the electrons freeze into an emergent lattice as a result of long-range Coulomb repulsion [7, 18]. Although a Wigner crystal is electrically insulating due to pinning of the electron lattice by disorder, domains, or the moiré lattice itself, the compressibility of the Wigner crystal is expected to be large and negative due to long-range Coulomb interactions [46]. Unlike DC transport, compressibility is one of the few techniques which is capable of providing positive evidence of Wigner crystallization. In our measurements, the compressibility decreases at commensurate filling while remaining positive and non-diverging, implying the likely formation of an energy gap and not a highly (negatively) compressible phase expected for an ideal Wigner crystal. However, unlike the conventional case, if the moiré potential strongly pins the electron lattice, it may be possible to form a thermodynamic energy gap [47]. We also cannot rule out the possibility of such a Wigner crystal and another gapped phase coexisting via phase separation as has been speculated to occur in GaAs bilayers [48]. Additionally, it may be possible to interpret the multiple density of states peaks as arising from differential strain between the two twisted bilayer graphene layers [49].

Although many band structure calculations predict narrow low energy bands between 5 and 10 meV [1–3, 5, 13], recent focus on lattice relaxation effects have brought estimates closer to experiment (∼20 meV) [50, 51], however, at least one other lattice relaxation model predicts a narrowing of the bandwidth as compared to unrelaxed calculations [52]. Our data support a bandwidth in the range of 25 to 45 meV, suggesting that the non-interacting band structure is not as narrow as anticipated by theory, leading to larger values of kinetic energy. This suggests that, in the creation of the correlated insulating states, the kinetic energy may play a more substantive role than many single-particle calculations imply. Moreover, as recently proposed [19], it is possible that the interaction effects are also strongly enhanced by a power-law diverging van Hove singularity.

In summary, we used compressibility measurements to access the shift of the chemical potential as the low-energy band structure is filled. We report a reduced Fermi velocity, a wide ∼35 meV bandwidth compared with many electronic structure calculations, and measure the gap widths at $n_s/4$ and $n_s/2$. The incompressible features at commensurate filling show essentially no field evolution up to 3 T before becoming obscured by other field-induced gaps. We do not observe strong Landau quantization at low magnetic field around commensurate filling, but at larger magnetic field we detect "Hofstadter" gaps that differ from previous transport studies [20, 21, 24].

We acknowledge useful discussions with Brian Skinner, Stevan Nadj-Perge, Philip W. Phillips, Bikash Padhi, Liang Fu, A.F. Young, V. Fatemi, D.S. Wei, and J.D. Sanchez-Yamagishi. In this work, sample fabrication (Y.C. and P.J.H.) was primarily supported by the National Science Foundation (NSF: DMR-1809802) and the Gordon and Betty Moore Foundation's EPiQS Initiative through grant GBMF4541. Capacitance measurements (S.L.T., A.D and R.C.A.) were supported by the STC Center for Integrated Quantum Materials, NSF grant number DMR-1231319. K.W. and T.T. acknowledge support from the Elemental Strategy Initiative conducted by the MEXT, Japan, A3 Foresight by JSPS and the CREST (JPMJCR15F3), JST. This work made use of the Materials Research Science and Engineering Center Shared Experimental Facilities supported by the NSF (DMR-0819762) and of Harvard's Center for Nanoscale Systems, supported by the NSF (ECS-0335765).

[1] E. Suárez Morell, J. D. Correa, P. Vargas, M. Pacheco, and Z. Barticevic, Phys. Rev. B **82**, 121407(R) (2010).
[2] Trambly de Laissardière, G. and Mayou, D. and Magaud, L., Nano Lett. **10**, 804 (2010).
[3] R. Bistritzer and A. H. MacDonald, Proc. Natl. Acad. Sci. U. S. A. **108**, 12233 (2011).
[4] G. Li, A. Luican, J. Loopes dos Santos, A. Castro Neto, A. Reina, J. Kong, and E. Andrei, Nature Physics **6**, 109 (2010).
[5] Y. Cao, V. Fatemi, A. Demir, S. Fang, S. L. Tomarken, J. Y. Luo, J. D. Sanchez-Yamagishi, K. Watanabe, T. Taniguchi, E. Kaxiras, R. C. Ashoori, and P. Jarillo-Herrero, Nature **556**, 80 (2018).
[6] V. Y. Irkhin and Y. N. Skryabin, JETP Lett. **107**, 651 (2018).
[7] B. Padhi, C. Setty, and P. W. Phillips, Nano Lett. **18**, 6175 (2018).
[8] M. Ochi, M. Koshino, and K. Kuroki, Phys. Rev. B **98**, 081102(R) (2018).
[9] A. Thomson, S. Chatterjee, S. Sachdev, and M. S. Scheurer, Phys. Rev. B **98**, 075109 (2018).
[10] J. Dodaro, S. Kivelson, Y. Schattner, X. Sun, and C. Wang, Phys. Rev. B **98**, 075154 (2018).
[11] X. Y. Xu, K. Law, and P. A. Lee, Phys. Rev. B **98**, 121406(R) (2018).
[12] M. Koshino, N. F. Q. Yuan, T. Koretsune, M. Ochi, K. Kuroki, and L. Fu, Phys. Rev. X **8**, 031087 (2018).
[13] J. Kang and O. Vafek, Phys. Rev. X **8**, 031088 (2018).
[14] H. C. Po, L. Zou, A. Vishwanath, and T. Senthil, Phys. Rev. X **8**, 031089 (2018).
[15] C.-C. Liu, L.-D. Zhang, W.-Q. Chen, and F. Yang, Phys. Rev. Lett. **121**, 217001 (2018).
[16] H. Isobe, N. F. Yuan, and L. Fu, Phys. Rev. X **8**, 041041 (2018).
[17] G. Tarnopolsky, A. J. Kruchkov, and A. Vishwanath, Phys. Rev. Lett. **122**, 106405 (2019).
[18] B. Padhi and P. Phillips, (2018), arXiv:1810.00884.
[19] N. F. Yuan, H. Isobe, and L. Fu, (2019), arXiv:1901.05432.

[20] Y. Cao, V. Fatemi, S. Fang, K. Watanabe, T. Taniguchi, E. Kaxiras, and P. Jarillo-Herrero, Nature **556**, 43 (2018).

[21] M. Yankowitz, S. Chen, H. Polshyn, Y. Zhang, K. Watanabe, T. Taniguchi, D. Graf, A. F. Young, and C. R. Dean, Science , 1059 (2019).

[22] A. L. Sharpe, E. J. Fox, A. W. Barnard, J. Finney, K. Watanabe, T. Taniguchi, M. Kastner, and D. Goldhaber-Gordon, (2019), arXiv:1901.0352.

[23] H. Polshyn, M. Yankowitz, S. Chen, Y. Zhang, K. Watanabe, T. Taniguchi, C. R. Dean, and A. F. Young, (2019), arXiv:1902.00763.

[24] X. Lu, P. Stepanov, W. Yang, M. Xie, M. A. Aamir, I. Das, C. Urgell, K. Watanabe, T. Taniguchi, G. Zhang, A. Bachtold, A. H. MacDonald, and D. K. Efetov, (2019), arXiv:1903.06513.

[25] A. Kerelsky, L. McGilly, D. M. Kennes, L. Xian, M. Yankowitz, S. Chen, K. Watanabe, T. Taniguchi, J. Hone, C. Dean, A. Rubio, and A. N. Pasupathy, (2018), arXiv:1812.08776.

[26] Y. Choi, J. Kemmer, Y. Peng, A. Thomson, H. Arora, R. Polski, Y. Zhang, H. Ren, J. Alicea, G. Rafael, F. von Oppen, K. Watanabe, T. Taniguchi, and S. Nadj-Perge, (2019), arXiv:1901.02997.

[27] K. Kim, M. Yankowitz, B. Fallahazad, S. Kang, H. C. Movva, S. Huang, S. Larentis, C. M. Corbet, T. Taniguchi, K. Watanabe, S. K. Banerjee, B. J. LeRoy, and E. Tutuc, Nano. Lett. **16**, 1989 (2016).

[28] Y. Cao, J. Luo, V. Fatemi, S. Fang, J. Sanchez-Yamagishi, K. Watanabe, T. Taniguchi, E. Kaxiras, and P. Jarillo-Herrero, Phys. Rev. Lett. **117**, 116804 (2016).

[29] See Supplemental Material for sample preparation details, which includes Refs. [5, 20, 28, 53].

[30] S. Luryi, Appl. Phys. Lett. **52**, 501 (1988).

[31] R. Goodall, R. Higgins, and J. Harrang, Phys. Rev. B **31**, 6597 (1985).

[32] See Supplemental Material for measurement and analysis details, which includes Refs. [54, 55].

[33] Y.-H. Zhang, H. C. Po, and T. Senthil, (2019), arXiv:1904.10452.

[34] Y. Zhang, Z. Jiang, J. Small, M. Purewal, Y.-W. Tan, M. Fazlollahi, J. Chudow, J. Jaszczak, H. Stormer, and P. Kim, Phys. Rev. Lett. **96**, 136806 (2006).

[35] Z. Jiang, Y. Zhang, H. Stormer, and P. Kim, Phys. Rev. Lett. **99**, 106802 (2007).

[36] J. G. Checkelsky, L. Li, and N. Ong, Phys. Rev. Lett. **100**, 206801 (2008).

[37] Y. Zhao, P. Cadden-Zimansky, Z. Jiang, and P. Kim, Phys. Rev. Lett. **104**, 066801 (2010).

[38] A. Young, C. Dean, L. Wang, H. Ren, P. Cadden-Zimansky, K. Watanabe, T. Taniguchi, J. Hone, K. Shepard, and P. Kim, Nat. Phys. **8**, 550 (2012).

[39] B. Hunt, J. Li, A. Zibrov, L. Wang, T. Taniguchi, K. Watanabe, J. Hone, C. Dean, M. Zaletel, R. Ashoori, and A. Young, Nat. Commun. **8**, 948 (2017).

[40] D. R. Hofstadter, Phys. Rev. B **14**, 2239 (1976).

[41] G. Wannier, Phys. Status Solidi B **88**, 757 (1978).

[42] C. R. Dean, L. Wang, P. Maher, C. Forsythe, F. Ghahari, Y. Gao, J. Katoch, M. Ishigami, P. Moon, M. Koshino, T. Taniguchi, K. Watanabe, K. L. Shepard, J. Hone, and P. Kim, Nature **497**, 598 (2013).

[43] L. Ponomarenko, R. Gorbachev, G. Yu, D. Elias, R. Jalil, A. Patel, A. Mishchenko, A. Mayorov, C. Woods, J. Wallbank, M. Mucha-Kruczynski, B. Piot, M. Potemski, I. Grigorieva, K. Novoselov, F. Guinea, V. Fal'ko, and A. Geim, Nature **497**, 594 (2013).

[44] B. Hunt, J. D. Sanchez-Yamagishi, A. F. Young, M. Yankowitz, B. J. LeRoy, K. Watanabe, T. Taniguchi, P. Moon, M. Koshino, P. Jarillo-Herrero, and R. C. Ashoori, Science , 1427 (2013).

[45] K. Kim, A. DaSilva, S. Huang, B. Fallahazad, S. Larentis, T. Taniguchi, K. Watanabe, B. J. LeRoy, A. H. MacDonald, and E. Tutuc, Proc. Natl. Acad. Sci. U.S.A. **114**, 3364 (2017).

[46] M. Bello, E. Levin, B. Shklovskii, and A. Efros, Sov. Phys. JETP **80**, 1596 (1981).

[47] B. Padhi, Y. Yang, D. M. Ceperley, and P. W. Phillips, (private communication).

[48] D. Zhang, X. Huang, W. Dietsche, K. von Klitzing, and J. H. Smet, Phys. Rev. Lett. **113**, 076804 (2014).

[49] Z. Bi, N. F. Yuan, and L. Fu, (2019), arXiv:1902.10146.

[50] S. Carr, S. Fang, Z. Zhu, and E. Kaxiras, (2019), arXiv:1901.03420.

[51] N. R. Walet and F. Guinea, (2019), arXiv:1903.00340.

[52] P. Lucignano, D. Alfè, V. Cataudella, D. Ninno, and G. Cantele, Phys. Rev. B **99**, 195419 (2019).

[53] L. Wang, I. Meric, P. Y. Huang, Q. Gao, Y. Gao, H. Tran, T. Taniguchi, K. Watanabe, L. M. Campos, D. A. Muller, J. Guo, P. Kim, J. Hone, K. L. Shepard, and C. R. Dean, Science **342**, 614 (2013).

[54] J. P. Eisenstein, L. N. Pfeiffer, and K. W. West, Phys. Rev. Lett. **68**, 674 (1992).

[55] G. L. Yu, R. Jalil, B. Belle, A. S. Mayorov, P. Blake, F. Schedin, S. V. Morozov, L. A. Ponomarenko, F. Chiappini, S. Wiedmann, U. Zeitler, M. I. Katsnelson, A. K. Geim, K. S. Novoselov, and D. C. Elias, Proc. Natl. Acad. Sci. U. S. A. **110**, 3282 (2013).